HHS Public Access

Author manuscript

Curr Drug Targets. Author manuscript; available in PMC 2015 November 26.

Published in final edited form as:

Curr Drug Targets. 2015 ; 16(14): 1582–1590.

Multistage Nanovectors Enhance the Delivery of Free and Encapsulated Drugs

Jonathan O. Martinez[1,*,†], **Michael Evangelopoulos**[1,†], **Rohan Bhavane**[2], **Stefania Acciardo**[1,3], **Francesco Salvatore**[4,5], **Xuewu Liu**[1], **Mauro Ferrari**[1], and **Ennio Tasciotti**[1]

[1]Department of Nanomedicine, Houston Methodist Research Institute, Houston, TX

[2]Department of Pediatric Radiology, Texas Children's Hospital, Houston, TX

[3]Department of Mechanical and Aerospace Engineering, Politecnico di Torino, Turin, Italy

[4]CEINGE Advanced Biotechnology s.c.a.r.l, Via G. Salvatore 486, 80145 Naples, Italy

[5]Fondazione IRCCS SDN, Via Gianturco 113, 80143 Naples, Italy

Abstract

Nanoparticles have considerable potential for cancer imaging and therapy due to their small size and prolonged circulation. However, biological barriers can impede the delivery of a sufficient dose of a drug to the target site, thereby also resulting in the accumulation of toxic compounds within healthy tissues, and systemic toxicity. Multistage nanovectors (MSV) preferentially accumulate on inflamed endothelium, and can thus serve as carriers for drugs and nanoparticles. Herein, we describe the loading of free (i.e., melittin) and nano-encapsulated (i.e., doxorubicin-loaded micelles) drugs into MSV, and report the impact of surface charge and pore size on drug loading. For both drug formulations, negatively charged MSV (i.e., oxidized) with larger pores were shown to retain higher concentrations of payloads compared to positively charged (i.e., APTES-modified) MSV with small pores. Treatment of human umbilical vein endothelial cells (HU-VEC) with melittin-loaded MSV (MEL@MSV) resulted in an 80% reduction in cell viability after 3 days. Furthermore, MEL@MSV conjugated with anti-vascular endothelial growth factor receptor 2 (VEGFR2) antibodies displayed preferential targeting and delivery of MEL to activated HUVEC expressing VEGFR2. Treatment of HUVEC and MCF7 cells with doxorubicin-loaded micelles (DOXNP@MSV) resulted in a 23% and 47% reduction in cell viability, respectively. Taken together, these results demonstrate increased loading of a payload in oxidized, large pore MSV, and effective delivery of free and nano-encapsulated drugs to endothelial and cancer cells.

[*]Address correspondence to this author at the Houston Methodist Research Institute, 6670 Bertner Avenue MS R7-414, Houston, TX 77030-2602; Tel: 713-441-7264; Fax: 713-441-7438; jomartinez@HoustonMethodist.org.

[†]Both authors contributed equally to this work.

Conflict of Interest: Commercialization rights on the intellectual property presented in this paper have been acquired by Leonardo Biosys-tems, from the titleholder, The University of Texas Health Science Center in Houston. Mauro Ferrari is the founding scientist of Leonardo Biosystems, Ennio Tasciotti is the inventor of the technology and hereby both authors disclose potential financial interests. This work was supported financially by: the Department of Defense (W81XWH-12-10414), the NIH (1R21CA173579-01A1; 5U54CA143837), Italian Ministry of Health (RF-2010-2305526), and internal support provided by HMRI including the Ernest Cockrell Jr. Distinguished Endowed Chair.

supplementary Material: Supplementary material is available on the publisher's web site along with the published article.

Keywords

Doxorubicin; drug delivery; melittin; micelles; multistage nanovector; nanoparticles

1. introduction

Although nanotechnology has significantly improved the delivery of cancer therapeutics, only a few drugs have been successfully used in the clinical setting [1]. With more than 500,000 Americans expected to suffer from cancer this year [2], further advances in drug delivery and nanotechnology could drastically reduce cancer-related deaths. Although the discovery of the enhanced permeability and retention of small particles (e.g., 10-100 nm) has led to promising treatments [3], limitations still exist. For example, the efficacy of current cancer therapeutics is hindered by their non-specific distribution, poor bioavailability and solubility, as well as their potential to trigger drug resistance after repeated administration [4]. Consequently, there is a need for drug delivery vectors that selectively target tumor sites in order to minimize damage to healthy tissue.

Currently, patients undergoing cancer treatments are often administered a cocktail of drugs to inhibit further tumor growth; each anti-cancer drug has its own pharmacokinetic properties and toxicity [5, 6]. Doxorubicin (DOX) [7] and melittin (MEL) [8-11], which is the primary component of bee venom, are well-established therapeutics for cancer. Thanks to its topoisomerase II inhibition properties, DOX has been very successful in treating leukemia, Hodgkin's lymphoma, and various other solid tumors [7]. As an inhibitor of calmodulin, MEL inhibits the growth and clonogenicity of human leukemia cells [12] and the growth of lung tumor cells [13]. However, despite the anticancer properties of these two drugs, the efficacy of their free formulations is limited due: (i) to non-specific accumulation in healthy tissues, which results in severe systemic toxicity (e.g., cardiotoxicity [7, 14, 15]), and (ii) to their susceptibility to rapid degradation in the blood [16]. Nanoparticles have the potential to significantly minimize these limitations. For example, when formulated into liposomes, the potency of DOX was conserved and toxic side effects were substantially reduced [17-19]. Thus, nanoparticles (or nanovectors) may represent a unique solution with which to entrap therapeutics while circumventing the systemic toxicity typically associated with chemotherapeutics.

Multistage nanovectors (MSV) have many beneficial properties, namely, improved bioavailability [20], tunable drug solubility [21], and sustained release [22]. Designed to navigate the vasculature [23], their size and shape enhance margination [24] (i.e., the propensity to drift laterally) thereby promoting accumulation at the tumor vasculature [25]. Furthermore, given the possibility of engineering the pore size of MSV from 5 to 100 nm, nanoparticles of various sizes and shapes can be loaded [26] and their release rate finely tuned [27]. Additional changes to the surface of MSV opened an avenue for the covalent attachment of targeting moieties and drugs [28]. Moreover, the regulation of surface charge permits the simultaneous loading of multiple nanoparticles each carrying a different therapeutic load [22]. Given these features, MSV are able to transport, protect, and deliver concentrated doses of siRNA [29, 30] and chemotherapeutics [31] thereby effectively reducing the size of the tumor. Consequently, in addition to silicon's biocompatibility and

benign degradation byproducts [32-34], MSV that can entrap multiple payloads are well suited for drug delivery applications.

This article describes the loading of free MEL and DOX-loaded micelles (DOXNP) within MSV. The effect of free drug and nano-encapsulated drug on loading was studied using MSV of various pore sizes and surface charges. In addition, surface modification of MSV with VEGFR2 antibody was used to assess the ability to selectively target endothelial cells overexpressing VEGFR2. Herein, we demonstrate that MSV are versatile drug carriers capable of transporting and protecting various payloads while actively targeting tumor vasculature.

2. Materials & Methods

2.1. Materials

MEL, DOX, 3-(4,5-dimethylthiazol-2-yl)-2,5-diphenyltetrazolium bromide (MTT), Tris-HCl, Triton X-100, dimethyl sulfoxide (DMSO), Lipopolysaccharide (LPS), bovine serum albumin (BSA), and (3-aminoproply) triethoxysilane (APTES) were purchased from Sigma Aldrich (St. Louis, MO). Phosphate buffered saline (PBS), DMEM, fetal bovine serum (FBS), HEPES, and Alexa Fluor 555 Phalloidin were purchased from Invitrogen (Grand Island, NY). DyLight 555, Sulfo-SMCC, and methanol-formaldehyde were purchased from Thermo Pierce (Rockford, IL). Human umbilical vein endothelial cells (HU-VEC), EBM-2, and EGM-2 SingleQuots were purchased from Lonza (Basel, Switzerland) and MDA-MB-231 and MCF-7 were purchased from ATCC (Manassas, VA). Anti-human vascular endothelial growth factor receptor (VEGFR2) and IgG FITC monoclonal antibodies were purchased from R&D Systems (Minneapolis, MN) and VEC-TASHIELD Mounting Medium with DAPI from Vector Laboratories (Burlingame, CA). 3000 centricon centrifugal filter devices were purchased from Millipore (Billerica, MA) and 1,2-distearoyl-phosphatidylethanolamine-polyethylene glycol amino-200 (DSPE-PEG-NH_2) was purchased from Avanti Polar Lipids (Alabaster, AL).

2.2. MSV Fabrication and Surface Modification

3.2 μm hemispherical multistage silicon nanovectors (MSV) were fabricated as previously described [27]. The pore sizes of the MSV used were: small (SP; 3-5 nm), large (LP;20-40 nm), and XLP (extra large; 40-60 nm). MSV were oxidized and APTES-modified as previously described [32]. APTES-modified MSV were conjugated with an FITC antibody directed against human VEGFR2 (or IgG for untargeted control) by incubating both MSV and the antibody in a 10 mM PB solution containing Sulfo-SMCC for 2 hours at 4°C under mixing. MSV were then washed in PB three times to remove unconjugated antibody.

2.3. Loading of MSV with Therapeutics

The free amino groups on MEL were conjugated with DyLight 555 ester using routine N-hydroxysuccinimide chemistry and the conditions previously reported for dye conjugation [35]. Briefly, MEL was mixed with free dye in 10 mM phosphate buffer at pH 7.2, and the free dye was filtrated and removed using centricon centrifugal filters.

DOXNP were synthesized by adapting a previously published protocol [36]. Briefly, DOX was dissolved in 30% methanol and added to DSPE-PEG-NH_2 powder at a drug to lipid ratio of 1:10 (wt/wt). The DOX-lipid solution was dried in a vacuum oven to a thin film and then hydrated with PBS at 60°C under sonication to form DOXNP. Free drug was removed *via* dialysis against PBS. The size of DOXNP was measured using a Brookhaven 90Plus PALS using dynamic light scattering and transmission electron microscopy images were acquired using a JEOL JEM1230 using a voltage of 80 kV and 56 μA beam current housed within the Department of Molecular Virology and Microbiology at Baylor College of Medicine operated by Dr. Budi Utama (Rice University) on samples stained with 1% uranyl acetate. Quantification of DOX within micelles was determined by measuring fluorescence excitation and emission using a plate reader (Molecular Devices) set at 480 and 580 nm after incubation in 1% Triton X-100 solution for 45 minutes.

Conjugated MEL or DOXNP was loaded into dried MSV. Briefly, the therapeutic solutions were suspended in 50 μL of a 20 mM Tris-HCl or PBS and incubated with MSV for 30 minutes. MEL loaded into MSV (MEL@MSV) or DOXNP loaded into MSV (DOXNP@MSV) was separated from unloaded dye using centrifugation at 4000×g for 5 minutes and washed twice with water. Quantification of MEL loading in MSV was confirmed by measuring the fluorescence excitation and emission at 493 nm and 515 nm, and comparing the results to a standard curve. DOXNP loading in MSV was quantified after incubation with 1% Triton X-100, heated at 65°C for 45 minutes, centrifuged, after which the supernatant was measured for fluorescence of DOX as described earlier.

2.4. Cell Culture

HUVEC were maintained in EBM-2 media supplemented with EGM-2 SingleQuots, as recommended by the manufacturer. The activation of surface VEGFR2 on HUVEC was achieved by serum starvation for 18 hours followed by stimulation with 1 μg/mL of LPS or VEGF165 for 6 hours. MDA-MB-231 and MCF-7 were maintained in DMEM supplemented with 10% FBS and 1% penicillin/streptomycin.

2.5. Confocal Microscopy

Point scanning confocal microscopy was performed with an upright Leica TCS SP5 confocal microscope housed at The University of Texas Health Science Center's Institute of Molecular Medicine, which is equipped with multiline argon, 561 nm, 594 nm, and 633 nm lasers. MSV loaded with fluorescent therapeutics were imaged with confocal microscopy using a 63× oil objective.

2.6. Flow Cytometry

Flow cytometry of cells and MSV was performed using a Becton Dickinson FACSCalibur Flow Cytometer equipped with Cellquest housed at The University of Texas Health Science Center's Institute of Molecular Medicine capable of six parameter analysis equipped with 488 nm and 635 nm lasers. The loading of therapeutic agents into MSV and conjugation with anti-VEGFR2 was characterized using flow cytometry. Briefly, 0.5–1 $\times 10^6$ MSV were resuspended in 200 μL of water in PBS and placed into polystyrene tubes for analysis. The activation of VEGFR2 on HUVEC was evaluated after detaching cells with EDTA cell

dissociation buffer. HUVEC were then washed in PBS, resuspended in a solution containing 1% BSA and 25 mM HEPES in PBS, and then labeled with anti human-VEGFR2 or IgG for 30 minutes at 4°C. Control and activated HUVEC samples stained with anti-VEGFR2 or IgG were analyzed with flow cytometry and compared.

2.7. Immunocytochemistry

The VEGFR2 expression of HUVEC was analyzed by growing cells on glass coverslips in 6-well plates at 100,000 cells per well and activated as described earlier. Cells were then fixed in 2% methanol-free formaldehyde, permeabilized in 0.1% Trition X-100, and stained with human VEGFR2-FITC antibody in PBS containing 1% BSA. Cells were then mounted with VECTASHIELD Mounting Medium with DAPI. Cell imaging was performed with the Nikon Eclipse TE2000E Widefield Fluorescence Microscope, which is equipped with a Photometrics Cascade 512B EMCCD camera, housed at The University of Texas Health Science Center's Institute of Molecular Medicine.

The targeting of anti-VEGFR2 MSV was investigated using confocal microscopy. HUVEC were grown on coverslips and exposed to anti-VEGFR2 MSV or IgG MSV at a ratio of 1:10 (Cells:MSV) for one hour at 37°C. HUVEC were fixed and permeabilized as before and then stained with Alexa Fluor 555 phalloidin for 20 minutes at room temperature and mounted with VECTASHIELD Mounting Medium with DAPI.

2.8. MTT

HUVEC, MDA-MB-231, and MCF-7 cells were seeded in 96-well plates at 5000 cells/well in their appropriate media. After allowing the cells to adhere for 6 hours, the media was replaced with fresh media (for controls) or with media containing either empty MSV or therapeutic loaded MSV and left to grow in the incubator at 37°C and 5% CO_2. At pre-determined times the media was removed, replaced with media containing 0.5 mg/mL of MTT dye, and incubated at 37°C and 5% CO_2 for four hours. After incubation the media containing MTT dye was removed, wells were treated with DMSO for 30 minutes at room temperature, and then read for absorbance at 570 nm using the plate reader.

2.9. Statistical Analysis

Statistics were obtained using Prism GraphPad software. All values were compared using a two-way analysis of variance proceeded by a Bonferroni post-test to compare groups. For all cases asterisks denote the following: * for p values between 0.01 and 0.05, ** for values between 0.001 and 0.01, and *** for values below 0.001.

3. Results & Discussion

3.1. MEL Loading into MSV

A standard curve relating the concentration of dye-conjugated MEL to fluorescence intensity demonstrated a linear correlation between 0 and 40μg/mL, thereby enabling quantification of MEL loading into MSV (Fig. S1). The impact of surface charge (oxidized and APTES) and pore size (SP, 5 nm; LP, 20 nm) on the loading of MEL into MSV was assessed. As previously described [37], MSV exhibited a negative surface charge (i.e., zeta potential)

after oxidation and alternated between positive and negative charge after APTES and fluorescent dye modification, respectively (Fig. S2). Fig. (1) compares the impact of surface charge on MEL loading by calculating drug content and entrapment efficiency (Supplemental Equation 1 and 2). In oxidized MSV, there was a 2-fold increase of entrapped MEL, which favored LP across the tested concentrations with a maximum drug content ratio of 90% (Fig. 1A). In APTES MSV, on the other hand, there was a statistically significant difference at the medium and high dose of MEL that favored LP and SP MSV, respectively, and with a maximum drug content of only 45% (Fig. 1B). While there was a direct correlation between MEL entrapment and pore size in oxidized MSV, loading efficiency in APTES MSV was erratic, i.e., it differed between the two pore sizes at different drug concentrations. A comparison of the entrapment efficiency of MEL between the conditions (Fig. S3) revealed a loading efficiency greater than 45% in oxidized MSV at the lower concentrations, while loading efficiency was less than 30% in all APTES MSV (see Fig. 1A and B). Furthermore, despite incubation with higher amounts of MEL, oxidized LP incubated with 25 μg successfully loaded nearly double the amount of MEL than APTES MSV incubated with 50 μg, which indicates selective loading of MEL to negatively charged MSV.

Loading was confirmed using fluorescence microscopy and flow cytometry. The fluorescent signal was higher in oxidized MSV (Fig. 1C) than in APTES MSV (Fig. 1D). MEL was loaded uniformly throughout the MSV in line with the typical shape of MSV, similar to fluorescent dye conjugations [35]. Similarly, at flow cytometry, loading was 19-fold higher in oxidized MSV than in APTES MSV, (Fig. S4). Previous reports established the preferential interactions of MEL with negatively charged surfaces or phospholipids [38, 39], thus supporting the increased loading of MEL we observed within oxidized MSV.

3.2. Endothelial Cell Response to Mel@MSV

HUVEC were continuously exposed to both oxidized and APTES SP and LP MSV loaded with MEL (i.e., MEL@MSV). The metabolic activity or viability of HUVEC treated with MEL@MSV at three cell:MSV ratios (LOW, 1:5; MED, 1:10; HIGH, 1:20) was monitored for three days using the MTT assay (Fig. 2). Previous data demonstrated that, at these ratios, MSV did not significantly affect HU-VEC viability [22, 33, 34]. Oxidized MSV displayed a substantial decrease in HUVEC viability upon treatment with MEL@MSV. The viability of HUVEC treated with oxidized SP marginally decreased at day 2, and was approximately 20% at LOW and MED ratios, and significantly decreased (35%) at a HIGH ratio (Fig. 2A). At day 3, the viability of HUVEC was significantly decreased (>50%) at all three ratios tested (Fig. 2A). Delivery of MEL@MSV with oxidized LP rapidly decreased the viability of HUVEC (> 60%) after a single day at all three ratios (Fig. 2B). The viability of HUVEC treated with LP MEL@MSV continued decrease significantly in the next two days, eventually resulting in an 80% decrease in viability (Fig. 2B). On the other hand, treatment of both SP and LP APTES MSV with MEL@MSV failed to trigger a significant reduction in cell viability in HUVEC at all three ratios tested (Fig. 2C,D). APTES SP and LP reduced cell viability by only 25% and 20%, respectively, by day 3, respectively. Hence, oxidized MSV enhanced delivery of MEL thereby triggering a significant decrease in the metabolic

activity of HUVEC. Consequently, MEL@MSV is able to deliver concentrated doses of MEL that induce cellular death.

3.3. Vegfr2-Targeted Delivery of Mel@MSV

HUVEC were activated to express VEGFR2 and were characterized using flow cytometry and fluorescence microscopy. An intense signal originated from the surface of HU-VEC (Fig. S5), and the cells maintained VEGFR2 expression while in culture (Fig. S6). APTES LP MSV was conjugated with human anti-VEGFR2 or anti-IgG FITC labeled antibodies. Successful conjugation of anti-VEGFR2/IgG and retention of MEL in MSV was investigated using flow cytometry and fluorescence microscopy (Fig. 3A-C). At flow cytometry, the fluorescence of surface functionalization of MSV with anti-VEGFR2 antibody was four-fold higher versus unmodified MSV, thereby confirming successful functionalization (Fig. 3A). For further confirmation, we direct the reader to previous work by our group demonstrating the successful functionalization of antibody through Fourier transform infrared spectroscopy and surface charge analysis [40].

The ability of antibody conjugated MSV to retain a pay-load was investigated using MEL as a model cargo. As shown in Fig. (3B), MSV with both anti-VEGFR2 and anti-IgG were consistently labeled. The signal from MEL co-localized with the antibody signal (Fig. 3B; note the strong orange fluorescence). Quantitative analysis of the simultaneous loading and antibody labeling of MSV, demonstrated preserved conjugation of both anti-VEGFR2 and anti-IgG after successful loading with similar amounts of MEL (Fig. 3C). Although MEL loading was best in oxidized MSV (Fig. S7), surface modification with antibodies exhibited 40% of the maximum load displayed by oxidized MSV and an increase in MEL retention exceeding 50-fold versus controls. Thus, the successful loading of MEL illustrated that MSV conserved the ability to load and retain a therapeutic payload upon conjugation with targeting antibodies.

Previous investigations demonstrated that decorating MSV with anti-VEGFR2 antibodies resulted in increased docking and firm adhesion towards VEGFR2-expressing cells [40]. Herein, targeted (i.e., anti-VEGFR2) and untargeted (i.e., anti-IgG) MSV were exposed to normal and activated (i.e., increased expression of VEGFR2) HUVEC. Fluorescence microscopy images after one hour revealed minimal MSV targeting by untargeted MSV in both conditions (Fig. 3D), whereas MSV targeting by targeted MSV was marginally higher in response to activated HUVEC (Fig. 3D). Three-dimensional confocal microscopy confirmed that MSV had successfully targeted HUVEC, which were found near the surface either docked (Fig. 3E, orange arrows) to expressed VEGFR2 or internalized (Fig. 3E, white arrows).

The viability of activated HUVEC after treatment with untargeted and targeted MEL@MSV for one hour at three ratios (LOW, MED, and HIGH) was measured after three days by means of the MTT assay (Fig. 3F). Untargeted MEL@MSV had a negligible impact on the viability of HUVEC; in fact, it caused only a 15% decrease in viability across the various ratios tested. However, targeted MEL@MSV decreased cell viability by more than 40%, and exhibited significant differences between the untargeted groups at all ratios tested. Comparison between Fig. (2B and 3F) demonstrated an apparent decrease in cell death (i.e.,

lower cytotoxicity) upon antibody functionalization with anti-VEGFR2. This variance can be attributed to the lower loading of MEL observed in antibody functionalized MSV (Fig. S7) and the limited incubation time (1 hour versus continuous for Fig. 3F and Fig. 2B, respectively) necessary to model MSV targeting *in vivo*. Hence, surface modification of MSV with anti-VEGFR2 antibodies enabled the selective delivery of MEL to endothelial cells overexpressing VEGFR2, which is a feature representative of tumor-associated vessels, and resulted in enhanced cellular death compared to MSV without targeting antibodies.

3.4. DOXNP Loading into MSV

Positively charged (i.e., cationic) DOXNP with sizes ranging from 10 to 20 nm (confirmed using dynamic light scattering (Fig. 4A) and transmission electron microscopy (Fig. 4B)) were synthesized and loaded into MSV. Loading was better into oxidized MSV for both SP and XLP MSV, for which there were 7- and 18-fold increases, respectively (Fig. 4C,D). DOXNP loading into XLP was 7-fold higher than in SP MSV, due to the small pores (3-5 nm) that obstructed efficient loading. Furthermore, the loading of fluorescent micelles was similar to that of DOXNP being higher in oxidized and XLP MSV (Fig. S8), and confirms that the MSV surface (rather than the encapsulated payload) was a major factor for efficient loading of payloads. Fluorescence micrographs showed a homodisperse DOX signal throughout the MSV, which confirmed consistent loading of DOXNP (Fig. 4E-G and S9). Furthermore, MSV displayed a burst release of 67% and 58% DOXNP within the first hour in the case of SP and XLP, respectively (Fig. 4E). After the initial delivery, the discharge of DOXNP from MSV decreased substantially, i.e., the payload release for SP and XLP was 2% and 7%, respectively, at two hours (Fig. 4H).

The loading of cationic micelles into oxidized MSV confirmed the role of electrostatics in the loading of MSV with nanoparticles [22], thus illustrating the flexibility of MSV for loading a variety of payloads with distinct surface properties. The successful loading of DOXNP in negatively charged MSV (i.e., oxidized, fluorescent-dye conjugated and antibody-conjugated, Fig. 3C and Fig. S2) demonstrates the possibility of simultaneously loading DOX while retaining fluorescent recognition abilities for tracking the *in vivo* biodistribution [33, 35]. Furthermore, the ability to effortlessly engineer the surface chemistry and pore size of MSV can enable the simultaneous loading of various payloads into MSV with given properties, such as DOXNP and MEL into oxidized LP MSV.

3.5. Cell Viability Attributed to Doxnp@MSV

The ability of DOXNP@MSV to provide a therapeutic benefit was tested on two human cell lines: endothelial (HU-VEC) and breast cancer (MCF-7). The viability of both HUVEC and MCF-7 cells was assessed using the MTT assay during three days of continuous treatment with DOX, DOXNP, or DOXNP@MSV. The data were collected each day and normalized to the viability of the control (Fig. 5). DOX exerted a substantial effect on HUVEC (Fig. 5A) and MCF-7 (Fig. 5B) at both low (L, 0.73 μg) and high (H, 2.5 μg) doses. In general, larger increases in cell death were observed at the high dose compared to the low dose. The response of HUVEC to DOX was immediate for all groups; and cell viability was decreased by 40% and 50% decreases by day 1 at low and high doses, respectively (Fig. 5A).

However, in the case of the low dose, there was a lower cell death observed after day 1 in all the groups, which resulted in a 45-50% decrease in overall viability.

On the other hand, the high doses of DOX and DOXNP induced a 90% decrease in viability by day 3. DOXNP@MSV at the high dose modified the toxicity of DOX; in fact, at this dose DOXNP@MSV was associated with higher HUVEC viability, which indicates that the MSV abates the toxicity of DOX. Conversely, MCF-7 cells exhibited a gradual reaction to DOX at both doses (Fig. 5B). At the low dose, the viability of MCF-7 cells was reduced by 15% at day 1 and culminated in a final reduction of 40% by day 3. As with HUVEC, the high doses of DOX and DOXNP induced a more pronounced effect on MCF-7. DOXNP@MSV displayed more gradual decreases in metabolic activity although cell viability was higher compared to the other groups that confirm its ability to dampen the toxicity of DOX.

To illustrate the initial changes in MCF-7 cell viability induced by DOXNP@MSV, the day 1 values from Fig. (5A and B) were normalized to 100% for all groups (Fig. 5C, D). The viability of HUVEC treated with a low DOXNP@MSV dose differed negligibly between day 2 and day 3, while the high dose of DOXNP@MSV failed to exhibit a significant difference, as was observed with DOX and DOXNP (Fig. 5C). As observed with HUVEC, MCF-7 cells displayed a minor decrease in cell death of about 10% between day 2 and day 3 (Fig. 5D). Differently, the high dose caused a significant decrease in cell viability in the case of free DOX/DOXNP (70%) and DOXNP@MSV (50%); and there was a similar decrease of 25% in cell viability between day 2 and day 3 for all the groups. Although DOXNP@MSV initially abated the toxicity of DOX in MCF-7 cells, this analysis revealed that similar decreases in cell viability were triggered after the initial exposure to the treatment.

A possible explanation of the delayed DOXNP@MSV-induced death of MCF-7 cells compared to HUVEC could be attributed to the higher internalization of MSV in HU-VEC [41, 42] than in MCF-7. Previous reports have demonstrated delayed internalization exhibited by MCF-7 and other cancer cells for nano- and microparticles of various geometries, sizes, and materials [43, 44]. In fact, as shown in Fig. (6A), after four hours, MSV internalization (green) was only visible in HUVEC and was mainly localized in the peri-nuclear region, consistent with previous results [42]. Furthermore, after exposure to MSV, both HUVEC and MCF-7 (Fig. 6A and B, respectively) displayed a typical nuclear (blue) and f-actin microfilament (red) structure. HUVEC displayed organized microfilaments that extended parallel throughout the cytoplasm, while MCF-7 micro-filaments were less organized and occurred primarily around the cell boundaries. Thus, the low internalization rate experienced by MCF-7 could benefit the gradual release of DOXNP from MSV after the first hour of day 1 [31], thereby permitting delayed increases in the delivery of DOX outside of cells overtime, and explaining the gradual decreases in MCF-7 cell viability.

Conclusion

The ability to effectively load free drugs and nano-encapsulated drugs into a versatile nanovector can improve the delivery of drugs to the target site while minimizing toxicity on healthy cells. This study demonstrates better loading of free MEL and nano-formulated DOX in oxidized, LP MSV, and a direct relationship between drug loading and MSV pore size. This enhanced loading can be attributed to the overall increase in negatively charged surface area and the exclusion of larger payloads from SP MSV. Furthermore, when conjugated with anti-VEGFR2 antibody, MSV targeted the delivery of MEL to activated endothelial cells. DOXNP@MSV delayed cancer cell death, possibly because of the prolonged release of DOX from its porous matrix. Taken together, these results demonstrate: i) the versatility of MSV for loading various payloads; ii) that they are able entrap free and nano-encapsulated drugs; and iii) that they may enable the simultaneous loading of various payloads.

Supplementary Material

Refer to Web version on PubMed Central for supplementary material.

Acknowledgments

JOM and ME wrote the paper and analyzed the data. RB loaded melittin, fabricated micelles, quantified cellular viability and performed bioconjugation. ET performed flow cytometry and fluorescence imaging. SA collected data. FS edited the manuscript. XL fabricated multistage nanovectors. MF and ET provided research guidance, coordination and oversaw the research plan. The authors would like to also acknowledge Zhengmei Mao from The University of Texas Health Science Center at Houston's Brown Foundation Institute of Molecular Medicine for the Prevention of Human Diseases Microscopy Service Center for assistance with microscopy, David Haviland (HMRI) for flow cytometry assistance, Dr. Budi Utama (Rice University) for transmission electron miscrocopy imaging, and Jean Ann Gilder (Scientific Communication srl., Naples, Italy) and Julianna Kathryn Swartzenberg for assistance with manuscript preparation.

References

1. Zhang L, Gu FX, Chan JM, Wang AZ, Langer RS, Farokhzad OC. Nanoparticles in medicine: therapeutic applications anddevelopments. Clinical pharmacology and therapeutics. 2008; 83(5): 761–9. [PubMed: 17957183]
2. Siegel R, Naishadham D, Jemal A. Cancer statistics, 2013. CA Cancer J Clin. 2013; 63(1):11–30. [PubMed: 23335087]
3. Greish K. Enhanced permeability and retention (EPR) effect for anticancer nanomedicine drug targeting. Methods Mol Biol. 2010; 624:25–37. [PubMed: 20217587]
4. Deepa K, Singha S, Panda T. Doxorubicin nanoconjugates. Journal of nanoscience and nanotechnology. 2014; 14(1):892–904. [PubMed: 24730306]
5. Rugo HS, O'Shaughnessy JA, Perez EA. Clinical roundtable monograph. Current treatment options for metastatic breast cancer: what now? Clin Adv Hematol Oncol. 2011; 9(11):1–16.
6. Conroy T, Desseigne F, Ychou M, et al. FOLFIRINOX versus Gemcitabine for Metastatic Pancreatic Cancer. N Engl J Med. 2011; 364(19):1817–25. [PubMed: 21561347]
7. Carvalho C, Santos RX, Cardoso S, et al. Doxorubicin: the good, the bad and the ugly effect. Curr Med Chem. 2009; 16(25):3267–85. [PubMed: 19548866]
8. Havas LJ. Effect of bee venom on colchicine-induced tumours. Nature. 1950; 166(4222):567–8. [PubMed: 14780150]

9. Jo M, Park MH, Kollipara PS, et al. Anti-cancer effect of bee venom toxin and melittin in ovarian cancer cells through induction of death receptors and inhibition of JAK2/STAT3 pathway. Toxicol Appl Pharmacol. 2012; 258(1):72–81. [PubMed: 22027265]
10. Orsolic N. Bee venom in cancer therapy. Cancer Metastasis Rev. 2012; 31(1-2):173–94. [PubMed: 22109081]
11. Lee YJ, Kang SJ, Kim BM, Kim YJ, Woo HD, Chung HW. Cytotoxicity of honeybee (Apis mellifera) venom in normal human lymphocytes and HL-60 cells. Chem Biol Interact. 2007; 169(3):189–97. [PubMed: 17658502]
12. Hait WN, Grais L, Benz C, Cadman EC. Inhibition of growth of leukemic cells by inhibitors of calmodulin: phenothiazines and melittin. Cancer Chemother Pharmacol. 1985; 14(3):202–5. [PubMed: 3995682]
13. Zhu HG, Tayeh I, Israel L, Castagna M. Different susceptibility of lung cell lines to inhibitors of tumor promotion and inducers of differentiation. J Biol Regul Homeost Agents. 1991; 5(2):52–8. [PubMed: 1910248]
14. Tacar O, Sriamornsak P, Dass CR. Doxorubicin: an update on anticancer molecular action, toxicity and novel drug delivery systems. J Pharm Pharmacol. 2013; 65(2):157–70. [PubMed: 23278683]
15. Rinehart JJ, Lewis RP, Balcerzak SP. Adriamycin cardiotoxicity in man. Ann Intern Med. 1974; 81(4):475–8. [PubMed: 4277990]
16. Pan H, Soman NR, Schlesinger PH, Lanza GM, Wickline SA. Cytolytic peptide nanoparticles ('NanoBees') for cancer therapy. Wiley Interdiscip Rev Nanomed Nanobiotechnol. 2011; 3(3): 318–27. [PubMed: 21225660]
17. Balazsovits JA, Mayer LD, Bally MB, et al. Analysis of the effect of liposome encapsulation on the vesicant properties, acute and cardiac toxicities, and antitumor efficacy of doxorubicin. Cancer Chemother Pharmacol. 1989; 23(2):81–6. [PubMed: 2491964]
18. Gabizon A, Dagan A, Goren D, Barenholz Y, Fuks Z. Liposomes as *in vivo* carriers of adriamycin: reduced cardiac uptake and preserved antitumor activity in mice. Cancer Res. 1982; 42(11):4734–9. [PubMed: 7127308]
19. Mayer LD, Tai LC, Ko DS, et al. Influence of vesicle size, lipid composition, and drug-to-lipid ratio on the biological activity of liposomal doxorubicin in mice. Cancer Res. 1989; 49(21):5922–30. [PubMed: 2790807]
20. Prestidge CA, Barnes TJ, Lau CH, Barnett C, Loni A, Canham L. Mesoporous silicon: a platform for the delivery of therapeutics. Expert Opin Drug Deliv. 2007; 4(2):101–10. [PubMed: 17335408]
21. Salonen J, Laitinen L, Kaukonen AM, et al. Mesoporous silicon microparticles for oral drug delivery: Loading and release of five model drugs. J Control Release. 2005; 108(2-3):362–74. [PubMed: 16169628]
22. Tasciotti E, Liu X, Bhavane R, et al. Mesoporous silicon particles as a multistage delivery system for imaging and therapeutic applications. Nat Nanotechnol. 2008; 3(3):151–7. [PubMed: 18654487]
23. Gentile F, Chiappini C, Fine D, et al. The effect of shape on the margination dynamics of non-neutrally buoyant particles in two-dimensional shear flows. J Biomech. 2008; 41(10):2312–8. [PubMed: 18571181]
24. Chiappini C, Tasciotti E, Serda RE, Brousseau L, Liu X, Ferrari M. Mesoporous silicon particles as intravascular drug delivery vectors: fabrication, in-vitro, and in-vivo assessments. physica status solidi (c). 2011; 8(6):1826–32.
25. van de Ven AL, Kim P, et al. Rapid tumoritropic accumulation of systemically injected plateloid particles and their biodistribution. J Control Release. 2012; 158(1):148–55. [PubMed: 22062689]
26. Martinez JO, Brown BS, Quattrocchi N, Evangelopoulos M, Ferrari M, Tasciotti E. Multifunctional to multistage delivery systems: The evolution of nanoparticles for biomedical applications. Chin Sci Bull. 2012; 57(31):3961–71. [PubMed: 24587616]
27. Chiappini C, Tasciotti E, Fakhoury JR, et al. Tailored porous silicon microparticles: fabrication and properties. Chemphyschem. 2010; 11(5):1029–35. [PubMed: 20162656]
28. Parodi A, Quattrocchi N, van de Ven AL, et al. Synthetic nanoparticles functionalized with biomimetic leukocyte membranes possess cell-like functions. Nat Nanotechnol. 2013; 8(1):61–8. [PubMed: 23241654]

29. Shen J, Xu R, Mai J, et al. High capacity nanoporous silicon carrier for systemic delivery of gene silencing therapeutics. ACS Nano. 2013; 7(11):9867–80. [PubMed: 24131405]
30. Xu R, Huang Y, Mai J, et al. Multistage vectored siRNA targeting ataxia-telangiectasia mutated for breast cancer therapy. Small. 2013; 9(9-10):1799–808. [PubMed: 23293085]
31. Blanco E, Sangai T, Hsiao A, et al. Multistage delivery of chemotherapeutic nanoparticles for breast cancer treatment. Cancer Lett. 2013; 334(2):245–52. [PubMed: 22858582]
32. Martinez JO, Chiappini C, Ziemys A, et al. Engineering multistage nanovectors for controlled degradation and tunable release kinetics. Biomaterials. 2013; 34(33):8469–77. [PubMed: 23911070]
33. Martinez JO, Boada C, Yazdi IK, et al. Short and long term, *in vitro* and *in vivo* correlations of cellular and tissue responses to mesoporous silicon nanovectors. Small. 2013; 9(9-10):1722–33. [PubMed: 23255523]
34. Martinez JO, Parodi A, Liu X, Kolonin MG, Ferrari M, Tasciotti E. Evaluation of cell function upon nanovector internalization. Small. 2013; 9(9-10):1696–702. [PubMed: 23166049]
35. Tasciotti E, Godin B, Martinez JO, et al. Near-infrared imaging method for the *in vivo* assessment of the biodistribution of nanoporous silicon particles. Mol Imaging. 2011; 10(1):56–68. [PubMed: 21303615]
36. Tang N, Du G, Wang N, Liu C, Hang H, Liang W. Improving penetration in tumors with nanoassemblies of phospholipids and doxorubicin. J Natl Cancer Inst. 2007; 99(13):1004–15. Epub 2007/06/29. [PubMed: 17596572]
37. Martinez JO, Evangelopoulos M, Chiappini C, Liu X, Ferrari M, Tasciotti E. Degradation and biocompatibility of multistage nanovectors in physiological systems. J Biomed Mater Res A. 2014; 102(10):3540–9. [PubMed: 25269799]
38. Kleinschmidt JH, Mahaney JE, Thomas DD, Marsh D. Interaction of bee venom melittin with zwitterionic and negatively charged phospholipid bilayers: a spin-label electron spin resonance study. Biophys J. 1997; 72(2 Pt 1):767–78. [PubMed: 9017202]
39. Batenburg AM, van Esch JH, Leunissen-Bijvelt J, Verkleij AJ, de Kruijff B. Interaction of melittin with negatively charged phospholipids: consequences for lipid organization. FEBS Lett. 1987; 223(1):148–54. [PubMed: 3666135]
40. Martinez JO, Evangelopoulos M, Karun V, et al. The effect of multistage nanovector targeting of VEGFR2 positive tumor endothelia on cell adhesion and local payload accumulation. Biomaterials. 2014; 35(37):9824–32. [PubMed: 25176066]
41. Serda RE, Gu J, Burks JK, Ferrari K, Ferrari C, Ferrari M. Quantitative mechanics of endothelial phagocytosis of silicon microparticles. Cytometry A. 2009; 75(9):752–60. [PubMed: 19610127]
42. Serda RE, Gu J, Bhavane RC, et al. The association of silicon microparticles with endothelial cells in drug delivery to the vasculature. Biomaterials. 2009; 30(13):2440–8. [PubMed: 19215978]
43. Almeida PV, Shahbazi MA, Makila E, et al. Amine-modified hyaluronic acid-functionalized porous silicon nanoparticles for targeting breast cancer tumors. Nanoscale. 2014; 6(17):10377–87. [PubMed: 25074521]
44. Gratton SEA, Ropp PA, Pohlhaus PD, et al. The effect of particle design on cellular internalization pathways. Proc Natl Acad Sci USA. 2008; 105(33):11613–8. [PubMed: 18697944]

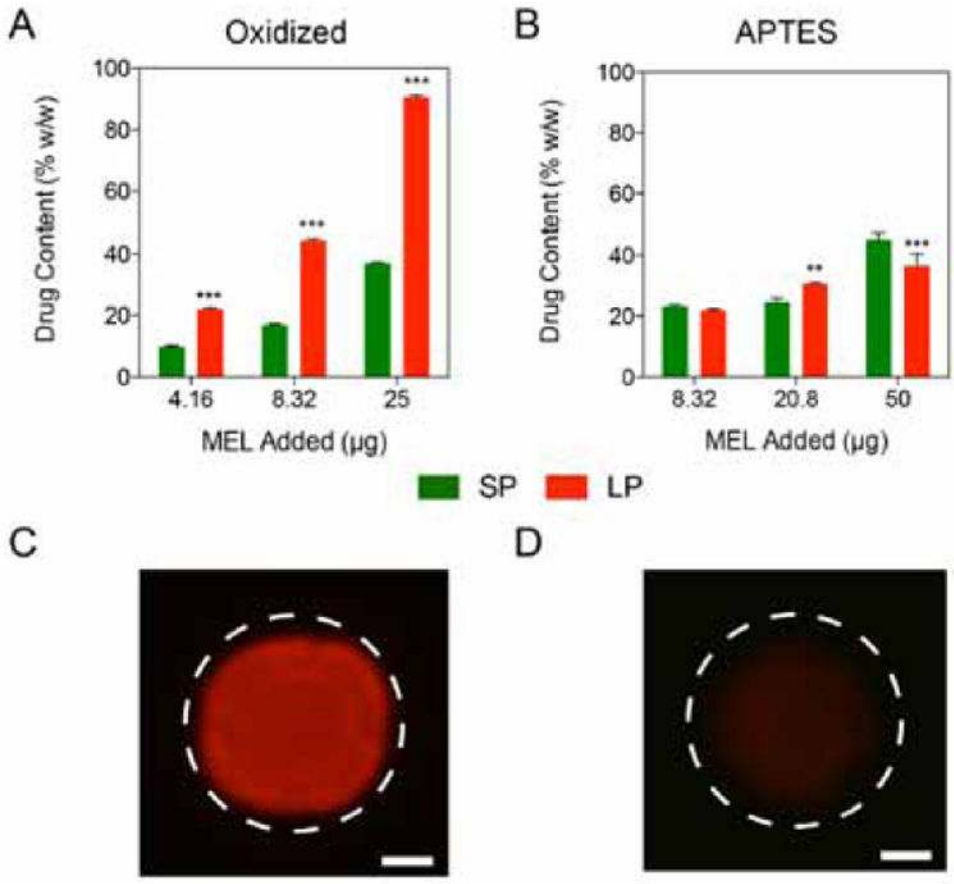

Fig. (1). Free melittin loading into MSV

A. Loading of MEL into oxidized and (**B**) APTES SP and LP MSV comparing the drug content (μg of MEL/μg of MSV). (** = $p < 0.01$, *** = $p < 0.001$) **C**. Fluorescent images of MEL loaded into oxidized and (**D**) APTES LP MSV, where white outline encircles the MSV (scale bar: 1 μm).

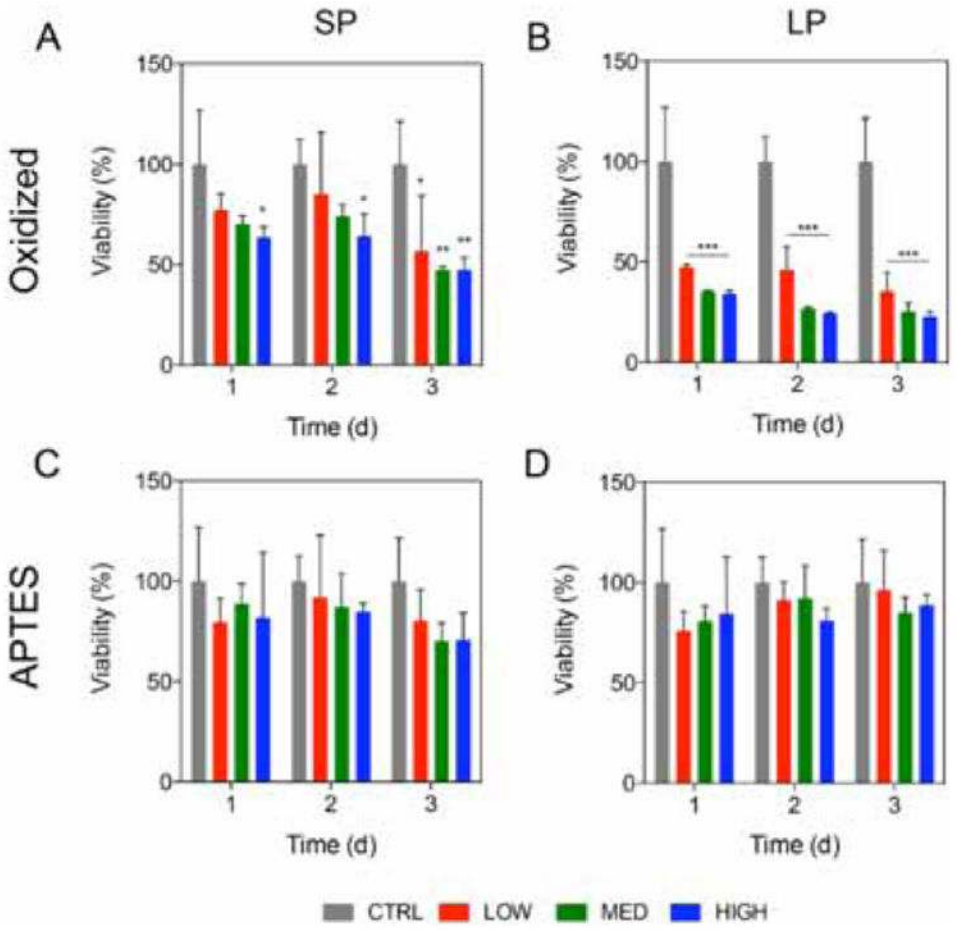

Fig. (2). Cellular proliferation of HUVEC upon treatment with MEL@MSV

A. MTT assay to evaluate the cell viability of HUVEC treated with oxidized SP and (**B**) LP MEL@MSV at LOW, MED, and HIGH concentrations corresponding to HUVEC to MSV ratios of 1:5, 1:10, and 1:20, respectively. **C**. HUVEC treated with APTES SP and (**D**) LP MEL@MSV at low, medium, and high. (* = $p < 0.05$, ** = $p < 0.01$, *** = $p < 0.001$).

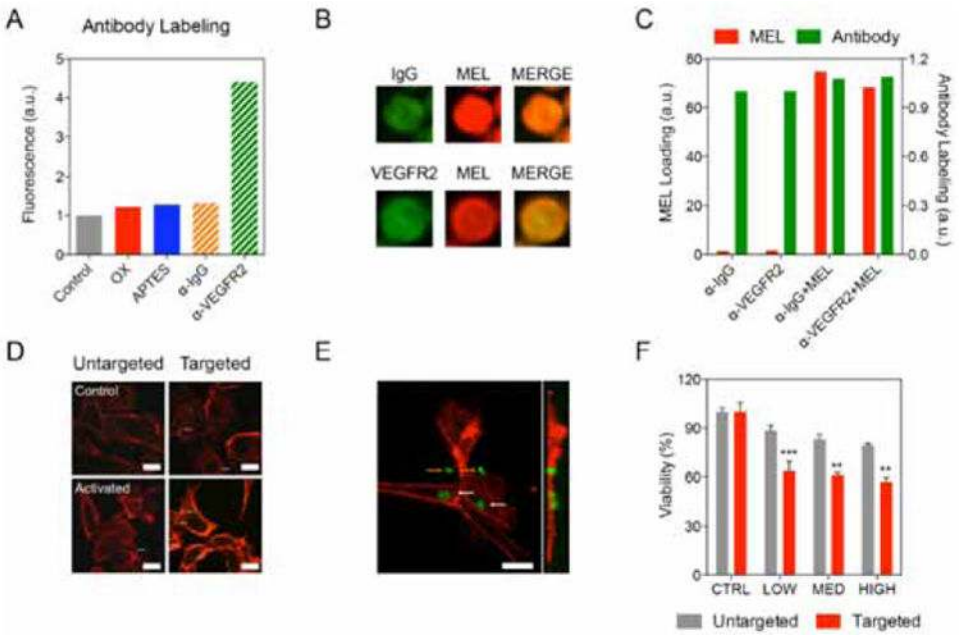

Fig. (3). Targeted delivery of MEL@MSV using a-VEGFR2 on activated HUVEC

A. Fluorescence of MSV measured by means of flow cytometry comparing oxidized, APTES, anti-IgG, and FITC anti-VEGFR2. **B**. Fluorescent microscopy images of anti-IgG MSV (upper, green) and anti-VEGFR2 MSV (bottom, green) loaded with MEL (red). **C**. Flow cytometry analysis of simultaneous MEL loading (red, left axis) and conserved antibody labeling (green, right axis) for both anti-IgG and anti-VEGFR2 MSV. **D**. Fluorescent microscopy images of control (top) and activated (bottom) HUVEC following treatment for 19 hours with untargeted (anti-IgG) and targeted (anti-VEGFR2) MSV. MSV are in green, microtubules (f-actin) in red, and white arrows indicate location of MSV. (scale bar, 25 μm). **E**. Docking (orange arrows) and internalization (white arrows) of targeted MSV on activated HUVEC. MSV are in green, microtubules (f-actin) in red. (scale bar, 25 μm). **F**. Cellular proliferation of activated HUVEC following treatment with untargeted and targeted MEL@MSV after three days comparing LOW (1:5), MED (1:10), and HIGH (1:20) ratios of MSV. (** = $p < 0.01$, *** = $p < 0.001$).

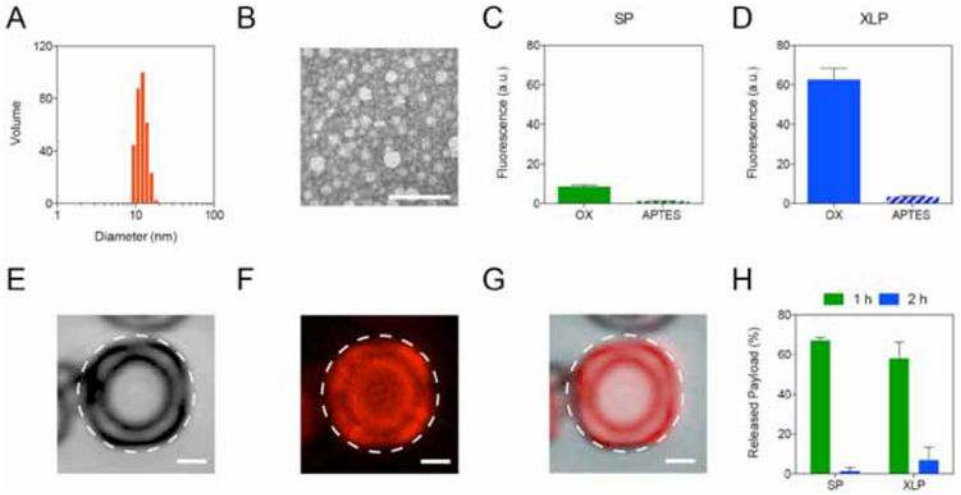

Fig. (4). DOXNP loading in MSV

A. Dynamic light scattering size analysis of DOXNP showing a mean diameter of 13 nm with sizes ranging from 10 to 20 nm. **B**. Transmission electron micrograph of DOXNP micelles showing nanoparticles of uniform size and shape. (scale bar, 100 nm). **C**. Quantitative analysis of cationic DOXNP loading into SP and (**D**) XLP comparing oxidized and APTES MSV. **E-G**. Fluorescent images of DOXNP@MSV showing (**E**) bright field, (**F**) DOX, and (**G**) merged channels. (scale bar, 1 μm) **H**. Release of DOXNP from MSV at 1 and 2 hours for SP and XLP.

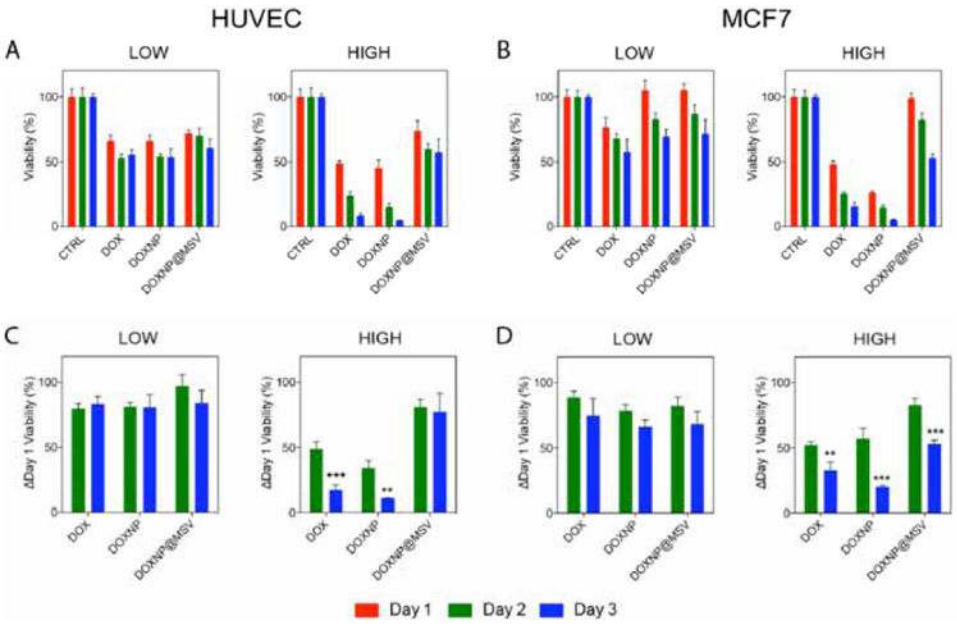

Fig. (5). Assessment of DOXNP@MSV toxicity on endothelial and cancer cells

A. Cell viability was measured using an MTT assay on HUVEC and (**B**) MCF-7 cancer cells after treatment with LOW and HIGH concentrations of DOX, DOXNP, and DOXNP@MSV and monitored for three days. **C**. Analysis of HUVEC and (**D**) MCF7 comparing day 2 and day 3 treatments normalized to day 1 treatments of the same group. (** = $p < 0.01$, *** = $p < 0.001$).

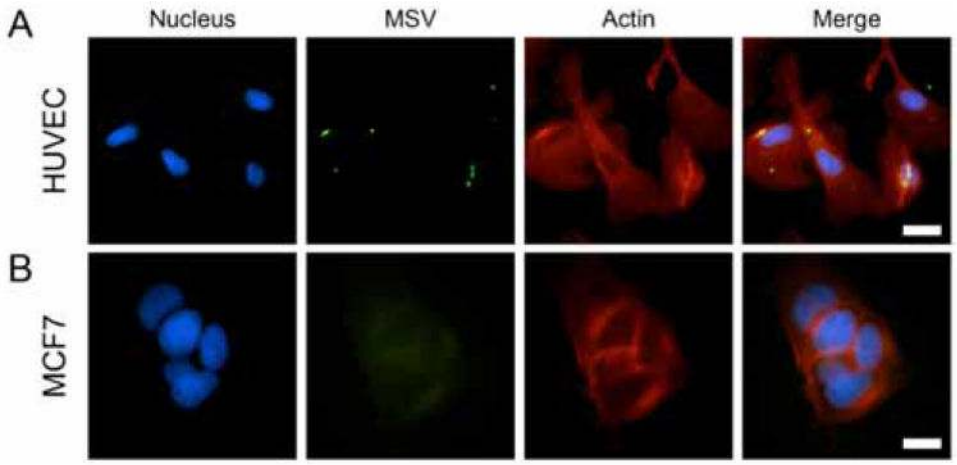

Fig. (6). Internalization of MSV on HUVEC and MCF7

Fluorescent images depicting nucleus (blue), MSV (green), microtubules (red), and merge of MSV internalized in HUVEC (**A**) and (**B**) MCF-7 (**B**) after 4 hours. (scale bar, 25 μm).